Journal of Electrostatics 114 (2021) 103619

Contents lists available at ScienceDirect

Journal of Electrostatics

journal homepage: www.elsevier.com/locate/elstat

Linear stability of electrocapillary convection in an infinite liquid layer

Kai-Xin Hu [a,*], Sheng Zheng [a], Cheng-Zhuo Zhao [a], Qi-Sheng Chen [b,c]

[a] Key Laboratory of Impact and Safety Engineering, Ministry of Education, School of Mechanical Engineering and Mechanics, Ningbo University, Ningbo, Zhejiang, 315211, China
[b] School of Engineering Science, University of Chinese Academy of Sciences, Beijing, 100190, China
[c] Key Laboratory of Microgravity, Institute of Mechanics, Chinese Academy of Sciences, Beijing, 100190, China

ARTICLE INFO

Keywords:
Electrohydrodynamics
Electrocapillary
Linear stability
Liquid layer

ABSTRACT

Electrocapillary convection is the flow driven by the interfacial shear stress induced by a surface-charge density and electric fields. It has become an important topic in electrohydrodynamics recently. The present work examine the convective instability for electrocapillary liquid layers by the modal and non-modal approaches. The modal analysis finds two kinds of modes, namely purely hydrodynamic and electrohydrodynamic modes, while both of them are stable. In the non-modal analysis, the amplifications of initial and external disturbances are measured by the transient growth and the response function, respectively. Both the perturbation velocity and surface-charge density can be amplified significantly.

1. Introduction

Electrohydrodynamics deals with the fluid motion induced by electric fields [1,2]. It has excited a wide range of interest for its importance in many practical applications, such as atomization of liquids [3], microfluidics [4] and increasing heat transfer in fluids [5,6]. There have been plenty of theoretical and experimental studies devoted to electrohydrodynamics, which have been reviewed by Melcher & Taylor [7], Saville [1] and Papageorgiou [8].

Electrocapillary flow is one of the most important fluid motions considered in electrohydrodynamics. It is driven by the interfacial shear stress induced by a surface-charge density and electric fields. The instabilities in electrocapillary flows have been studied by some authors. González et al. [9] have studied the influence of bounded geometry on electrocapillary instability both theoretically and experimentally. Petrin [10] has studied the electrocapillary instability of a conducting liquid cylinder by linear stability analysis. Mkrtchyan et al. [11] have presented an experimental study of the electrocapillary instability of magnetic fluid peak. The above works mainly restrict their attention to the interfacial instability, whose physical mechanism is well known: the surface deformation take places when the electrostatic force on the surface dominates the gravity and capillary force [12].

In many ways, the electrocapillary flow is similar to the thermocapillary flow, which is a kind of Marangoni convection caused by a temperature-induced surface tension gradient. Carrión, Herrada & Montanero [13] have studied numerically the influence of the dynamical free surface deformation on the stability of thermal convection in high-Prandtl-number liquid bridges. The free surface deformations caused by both the base flow and the perturbations are taking into account. Besides interfacial instabilities, there is another kind of instability in thermocapillary flows—convective instabilities, which are driven by mechanisms within the bulk of the layer and do not depend on the surface deformation [14]. The oblique hydrothermal wave is one of convective instabilities predicted by the modal stability theory. It has been observed in both experiments [15] and numerical simulations [16]. Energy analysis suggests that there are two kinds of mechanisms for convective instability, which are hydrodynamic and hydrothermal at small and large Prandtl numbers, respectively [17,18].

Recently, the investigation of convective instability has been extended from modal analysis to non-modal approach [19]. The former assumes a small perturbation varying exponentially with time and predicts the long-term behavior of disturbances. On the contrary, the latter focuses on the short-term characteristics of flow instabilities, including the transient energy growth and the behavior of response to external excitations [20]. The streamwise streaks (narrow regions where the streamwise velocity is larger or smaller than the average) predicted by the non-modal theory have been observed in many experiments of shear flows [21,22]. The investigations of non-modal stability have been generalized to non-Newtonian fluids [23–25] and electrohydrodynamic flows [26]. The works on thermocapillary convections [27] demonstrate

* Corresponding author.
E-mail address: hukaixin@nbu.edu.cn (K.-X. Hu).

https://doi.org/10.1016/j.elstat.2021.103619
Received 18 June 2021; Received in revised form 6 August 2021; Accepted 26 August 2021
Available online 4 September 2021

that rather large transient growths and responses can occur in subcritical flows.

When the gravity or capillary force is large enough, the interfacial instability is suppressed in the electrocapillary convection, while the convective instability may be preferred. However, to the best of our knowledge, the convective instability of electrocapillary convection has not been discussed in previous works. As the thermocapillary convection exhibits rich dynamic behaviors in its transition, one would expect that there may also be interesting phenomena and new mechanisms in electrocapillary convections. The purpose of this paper is examining the linear stability of electrocapillary liquid layers by modal and non-modal approaches, in order to understand their instabilities and transitions mechanism. The presence of gravity or capillary force makes the surface non-deformable, so only the convective instability is considered in the following.

The paper is organized as follows. In Section 2, we present the model of electrocapillary liquid layers, and derive the dimensionless governing equations. Theories of modal and non-modal analyses are introduced. Section 3 is dedicated to numerical results, including critical parameters, transient growths, response functions and pseudospectra. Section 4 is devoted to the discussion and comparisons with other flows. Finally, the conclusions are drawn in Section 5.

2. Mathematical formulation

2.1. Physical model

We consider two kinds of electrocapillary liquid layers, which are the linear flow and the return flow. The former has a linear velocity distribution, which can be realized on the layer placed on a horizontal plane. The latter with zero mass flux in the vertical section corresponds to the convection in a container. These two flows are convenient in the theoretical study.

The physical model of these two flows are presented in Fig. 1, where a film on a rigid plane is subjected to the Maxwell stress generated by the electric field on the interface. Here, *x, y, z* are the streamwise, spanwise and wall-normal direction, respectively. *d* is the depth, and $\widetilde{E}_x^b, \widetilde{E}_z^a$ are the tangential and vertical components of the electric field, respectively. When the variations of $\widetilde{E}_x^b, \widetilde{E}_z^a$ in the streamwise direction are not very obvious, we simply assume that $\widetilde{E}_x^b, \widetilde{E}_z^a$ are constants. This can be realized in the example shown in Fig. 2. Thus the flow is driven by a constant shear stress $\widetilde{T}_{zx} = \varepsilon_0 \widetilde{E}_x^b \widetilde{E}_z^a$.

Melcher & Taylor [7] have reported an experiment of electrocapillary convection shown in Fig. 2. When the film is shallow, the flow in the region far from two ends corresponds to the return flow in Fig. 1, which can be seen as follows.

In Fig. 2, the upper fluid (region (a)) is an insulating gas, and the lower one (region (b)) is a slightly conducting liquid filling an insulating container A. Electrodes B and C make electrical contact with the liquid to complete an electrical circuit with the source of potential V_0. F is a tilted electrode with one end in contact with electrode B. l is the length of the layer, and a is the height of left end of F. The distance between the interface and the tilted electrode is $h(x) = \frac{a}{l}\left(-x + \frac{l}{2}\right)$.

An electric field and surface charges are induced on the interface D. It is assumed that the electric field in this problem is quasi-static, and there is no bulk charge density. The tangential component of electric field is $\widetilde{E}_x^b = V_0/l$. As the electric field satisfies

$$\widetilde{\mathbf{E}} = -\nabla\widetilde{\psi}, \tag{2.1}$$

the electric potential on the interface is

$$\widetilde{\psi} = \frac{V_0}{l}\left(-\widetilde{x} + \frac{l}{2}\right). \tag{2.2}$$

Thus, the vertical component of electric field satisfies

$$\widetilde{E}_z^a = \frac{\widetilde{\psi}}{h} = \frac{V_0}{a}. \tag{2.3}$$

Due to Gauss' law in electrostatics, there is a relation between the vertical component of electric field and the surface-charge density $\widetilde{\vartheta}_0$: $\widetilde{E}_z^a = \frac{\widetilde{\vartheta}_0}{\varepsilon_0}$(There is also a surface-charge density on electrode F), which suggests that $\widetilde{\vartheta}_0 = \varepsilon_0 \frac{V_0}{a}$.

Then, the Maxwell stress is generated by the electric field. The interfacial shear stress is

$$\widetilde{\Gamma}_{zx} = \widetilde{\vartheta}_0 \widetilde{E}_x^b = \varepsilon_0 \widetilde{E}_z^a \widetilde{E}_x^b = \frac{\varepsilon_0 V_0^2}{la}, \tag{2.4}$$

which drives a convection in the liquid layer. Here, $\varepsilon_0 = 8.85 \times 10^{-12}$F/mis the vacuum permittivity. When $d << l$, the laminar flow in the region far from two ends is approximately parallel, so the velocity distribution is [7].

$$\widetilde{u}_0(z) = \frac{\varepsilon_0 V_0^2 d}{\mu la}\left(\frac{3}{4}\left(\frac{z}{d}\right)^2 - \frac{1}{2}\left(\frac{z}{d}\right)\right), \tag{2.5}$$

where$\mu$is the dynamic viscosity of liquid.

The scales of length, velocity, electric intensity, surface-charge density and interfacial shear stress are chosen as d, $\widetilde{U} = \frac{\varepsilon_0 V_0^2 d}{\mu la}$, $\widetilde{E} = \frac{V_0}{\sqrt{la}}$, $\widetilde{\vartheta} = \varepsilon_0 \frac{V_0}{a}$ and $\widetilde{\Gamma}_{zx} = \frac{\varepsilon_0 V_0^2}{la}$, respectively. The Reynolds number can be defined as $R = \rho \widetilde{U} d/\mu$. For 10 cSt silicone oil [28], the density $\rho = 0.93 \times 10^3$kg/m^3, the kinematic viscosity $\nu = \mu/\rho = 1 \times 10^{-5}$m^2/s, the surface tension $\Xi = 19.9 \times 10^{-3}$N/m. If we set $d \sim 0.04$m, $a \sim 0.04$m$V_0 \sim 1 \times 10^4$V, $l \sim 0.8$m, then $\widetilde{U} = \frac{\varepsilon_0 V_0^2 d}{\mu la} \sim 0.119$m/s, $R = \rho \widetilde{U} d/\mu \sim 500$. So in the following, the range of R we considered is 500–1500. The electrical conductivity of silicone oil has $\sigma \tilde{} 10^{-8}$S/m. However, if the functionalized graphene (FG) nanosheets are dispersed in the silicone oil, the electrical conductivity of FG-Silicone oil nanofluid increases to $\sigma = 1.5 \times$

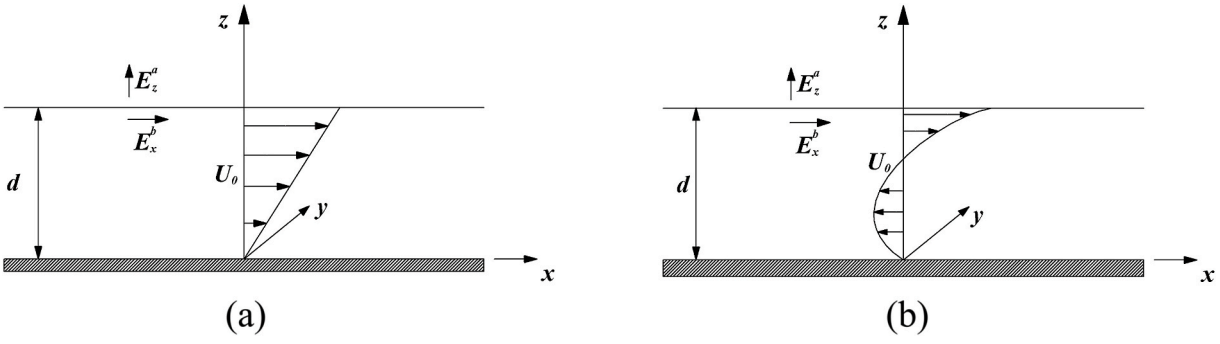

Fig. 1. Schematic of electrocapillary liquid layers: (a) the linear flow; (b) the return flow.

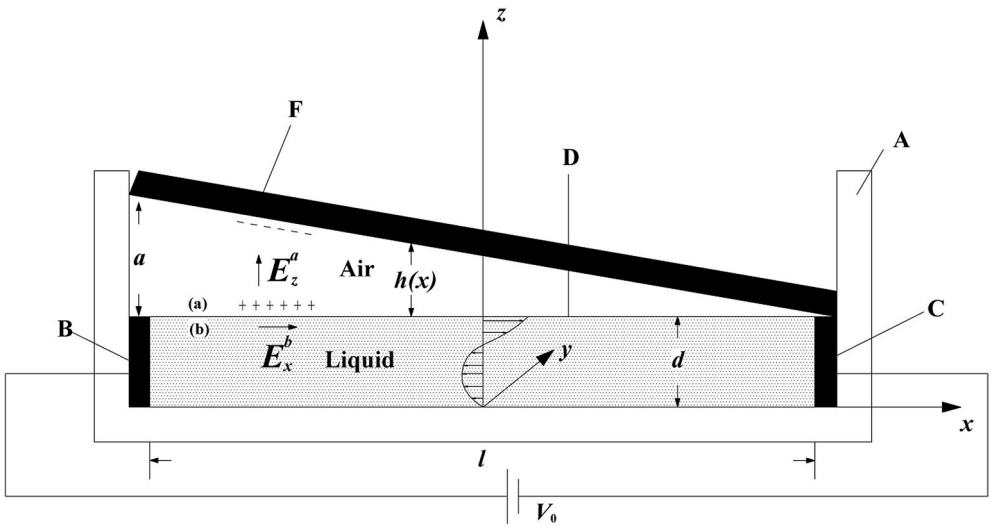

Fig. 2. A simple example of electrocapillary convection in an insulating container.

10^{-7}S/mwhen the weight fraction is 0.07% [29]. Then, the slightly conducting nanofluid prepared by dispersing nanoparticles into a dielectric base fluid can be used in the application of electrocapillary convections. The relative permittivity of silicone oil is $\varepsilon_r = 2.7$[30], so the free-charge density in the flow region decays with the bulk relaxation time $\tau = \varepsilon/\sigma = \varepsilon_r\varepsilon_0/\sigma \sim 1.59 \times 10^{-4}$s, which is much smaller than the time scale of flow$t_s = d/\widetilde{U} \sim 0.336$s. Thus, the effect of bulk charge density on the fluid motion will decay at once. The assumption of no bulk charge density is reasonable [7].

We do not consider the deformation of interface for three reasons. First, the magnitude of deformation on the surface can be measured by the capillary number: $Ca = \mu\widetilde{U}/\Theta$. For our estimated parameters, $Ca \approx 0.05 << 1$. Second, the typical deformation wavelength in the electrocapillary flow is well described in Rayleigh-Taylor instability theory by the capillary wavelength $\lambda_s = 2\pi\sqrt{\Xi/\rho g}$[9,31]. For the 10 cSt silicone oil, the corresponding dimensionless wavenumber is $d\sqrt{\rho g/\Xi} \approx 27$, which often causes high viscous dissipation and cannot lead to the instability. In addition, Melcher & Schwarz [32] suggested that when the gravity acts to stabilize the interface, the most critical wavelength of surface deformation is the longest one. However, $l >> \lambda_s \approx 9.28 \times 10^{-3}$min our case, which means that the surface instability is not preferred. Third, it is well known that the surface deformation only occurs when the electrostatic force on the surface dominates the gravity [9]. In our case, their ratio is $\frac{\varepsilon_0 V_0^2}{a^2}/(\rho g d) \approx 1.5 \times 10^{-3}$. Therefore, the assumption of a non-deformable surface can be satisfied.

In the model proposed by Melcher & Taylor [7] shown in Fig. 2, the convection of charge at the interface $\widetilde{U}\widetilde{\vartheta}_0$is negligible compared to the conduction current through the bulk $J_x \cdot d$, where $J_x = \frac{\sigma V_0}{l}$. Thus, the electric Reynolds number $R_e = \frac{l}{ad}\frac{\varepsilon_0\widetilde{U}}{\sigma} = \frac{\varepsilon_0^2 V_0^2}{\mu a^2 \sigma} << 1$and $\sigma >> \frac{\varepsilon_0^2 V_0^2}{\mu a^2} \sim 5.26 \times 10^{-10}$S/m. This condition can be satisfied for the FG-Silicone oil nanofluids.

2.2. Governing equations

The dimensionless forms of continuity equation and momentum equation can be expressed as follows,

$$\nabla \cdot \mathbf{u} = 0, \tag{2.6}$$

$$R\left(\frac{\partial \mathbf{u}}{\partial t} + \mathbf{u} \cdot \nabla \mathbf{u}\right) = -\nabla p + \nabla \cdot \boldsymbol{\tau}. \tag{2.7}$$

here$\mathbf{u}$, p and $\boldsymbol{\tau}$ stand for the velocity, pressure and stress tensor respectively. For Newtonian fluid,

$$\boldsymbol{\tau} = \mathbf{S}, \tag{2.8}$$

where $\mathbf{S} = \nabla\mathbf{u} + (\nabla\mathbf{u})^{\mathrm{T}}$is the strain-rate tensor.

For boundary conditions, there is no slip on the rigid plane,

$$u = v = w = 0, z = 0, \tag{2.9}$$

while on the surface,

$$w = 0, z = 1. \tag{2.10}$$

For the surface-charge density ϑ, we have$\vartheta = 0, z \neq 1$. Therefore, $\frac{\partial(w\vartheta)}{\partial z} = 0$. The conservation of charge leads to the following expression,

$$\frac{\partial \vartheta}{\partial t} + \frac{\partial(u\vartheta)}{\partial x} + \frac{\partial(v\vartheta)}{\partial y} + J_z = 0. \tag{2.11}$$

here, the current density in the vertical direction $J_z = \left(-O_h\frac{\partial \psi}{\partial z}\right)$ is caused by the Ohmic conduction, where $O_h = \widetilde{\sigma E}/\left(\frac{\widetilde{U}}{d}\widetilde{\vartheta}\right) = \frac{\mu a \sigma \sqrt{la}}{\varepsilon_0^2 V_0^2}$. For the FG-Silicone oil nanofluids mentioned above, O_h~1274.4.

The relation between the interfacial shear stress and electric field is

$$\Gamma_{zx} = \vartheta E_x^b, \quad \Gamma_{zy} = \vartheta E_y^b. \tag{2.12}$$

The basic flow is fully-developed, so the velocity field is supposed to be parallel,

$$\mathbf{u} = (U_0(z), 0, 0). \tag{2.13}$$

Hereafter, the subscript 0 stands for the basic flow. The solutions of linear flow and return flow can be derived by substituting (2.13) into governing equations as follows,

$$\text{Linear flow} U_0(z) = z, \tag{2.14}$$

$$\text{Return flow} U_0(z) = \frac{3}{4}z^2 - \frac{1}{2}z. \tag{2.15}$$

The velocity distributions above are displayed in Fig. 1.

When a small perturbation is added to the basic flow, the surface-charge density and the electric potential become $\vartheta = \vartheta_0 + \vartheta'$and $\psi = \psi_0 + \psi'$, respectively. The horizontal electric field $\mathbf{E}^b = -\nabla\psi$ has two components,

$$E_x^b = E_{x0}^b - \frac{\partial \psi'}{\partial x}, \tag{2.16}$$

$$E_y^b = -\frac{\partial \psi'}{\partial y}. \tag{2.17}$$

Thus, we can obtain the dimensionless forms of shear stress as follows,

$$T_{zx} = \vartheta E_x^b \approx 1 - \sqrt{\frac{l}{a}}\frac{\partial \psi'}{\partial x} + \vartheta', \tag{2.18}$$

$$T_{zy} = \vartheta E_y^b \approx -\sqrt{\frac{l}{a}}\frac{\partial \psi'}{\partial y}. \tag{2.19}$$

The linearized perturbation equation of surface-charge density is

$$\frac{\partial \vartheta'}{\partial t} + \left(\frac{\partial u'}{\partial x} + \frac{\partial v'}{\partial y}\right)\vartheta_0 + \frac{\partial \vartheta'}{\partial x}U_0 - O_h\frac{\partial \psi'}{\partial z} = 0. \tag{2.20}$$

In the dimensionless form, $\vartheta_0 = 1$.

As the flow region has no bulk charge density, the electric potential satisfies the Laplace equation,

$$\nabla^2 \psi' = 0. \tag{2.21}$$

2.3. Modal analysis

Suppose the perturbation has the normal mode form as follows,

$$(\mathbf{u}, \vartheta, p, \boldsymbol{\tau}, \psi) = (\mathbf{u}_0, \vartheta_0, p_0, \boldsymbol{\tau}_0, \psi_0) + \boldsymbol{\delta}, \tag{2.22a}$$

$$\boldsymbol{\delta} = (\widehat{u}, \widehat{v}, \widehat{w}, \widehat{\vartheta}, \widehat{p}, \widehat{\boldsymbol{\tau}}, \widehat{\psi})\exp[i(-\omega t + \alpha x + \beta y)]. \tag{2.22b}$$

Hereafter, the variables without subscript 0 stand for the perturbation. The mode has a complex frequency $\omega = \omega_r + i\omega_i$ and the wave numbers α, β in the x and y directions, respectively. We use the total wave number $k = \sqrt{\alpha^2 + \beta^2}$ and the propagation angle $\varphi = \tan^{-1}(\beta/\alpha)$ in the following.

The linearized perturbation equations can be derived,

$$i\alpha\widehat{u} + i\beta\widehat{v} + D\widehat{w} = 0, \tag{2.23}$$

$$\begin{aligned} &R[\beta(\widehat{w}DU_0 + U_0 i\alpha\widehat{u}) - \alpha(U_0 i\alpha\widehat{v})] \\ &-\beta\left(i\alpha\widehat{\tau}_{11} + i\beta\widehat{\tau}_{12} + D\widehat{\tau}_{13}\right) + \alpha\left(i\alpha\widehat{\tau}_{12} + i\beta\widehat{\tau}_{22} + D\widehat{\tau}_{23}\right) = Ri\omega(\beta\widehat{u} - \alpha\widehat{v}), \end{aligned} \tag{2.24}$$

$$\begin{aligned} &R\alpha\left(D\widehat{w}\cdot DU_0 + \widehat{w}D^2U_0 + DU_0\cdot i\alpha\widehat{u} + U_0 i\alpha D\widehat{u}\right) + R\beta(DU_0\cdot i\alpha\widehat{v} + U_0 i\alpha D\widehat{v}) \\ &-Rik^2(U_0 i\alpha\widehat{w}) - \left(i\alpha^2 D\widehat{\tau}_{11} + 2i\alpha\beta D\widehat{\tau}_{12} + \alpha D^2\widehat{\tau}_{13} + i\beta^2 D\widehat{\tau}_{22} + \beta D^2\widehat{\tau}_{23}\right) \\ &+ik^2\left(i\alpha\widehat{\tau}_{13} + i\beta\widehat{\tau}_{23} + D\widehat{\tau}_{33}\right) = Ri\omega\left(\alpha D\widehat{u} + \beta D\widehat{v} - ik^2\widehat{w}\right), \end{aligned} \tag{2.25}$$

$$\widehat{\tau}_{11} - 2i\alpha\widehat{u} = 0,\ \widehat{\tau}_{12} - (i\alpha\widehat{v} + i\beta\widehat{u}) = 0,\ \widehat{\tau}_{13} - (D\widehat{u} + i\alpha\widehat{w}) = 0, \tag{2.26}$$

$$\widehat{\tau}_{22} - (2i\beta\widehat{v}) = 0,\ \widehat{\tau}_{23} - (i\beta\widehat{w} + D\widehat{v}) = 0,\ \widehat{\tau}_{33} - (2D\widehat{w}) = 0. \tag{2.27}$$

$$D^2\widehat{\psi} - (\alpha^2 + \beta^2)\widehat{\psi} = 0. \tag{2.28}$$

here, $D = \frac{d}{dz}$. The boundary conditions on the plane $z = 0$ are

$$\widehat{u} = \widehat{v} = \widehat{w} = 0, \tag{2.29}$$

while on the surface $z = 1$, there are

$$\widehat{\tau}_{13} + i\alpha S_a\widehat{\psi} - \widehat{\vartheta} = 0,\ \widehat{\tau}_{23} + i\beta S_a\widehat{\psi} = 0,\ \widehat{w} = 0, \tag{2.30}$$

$$i\alpha\widehat{u} + i\beta\widehat{v} + i\alpha U_0\widehat{\vartheta} - O_h D\widehat{\psi} = i\omega\widehat{\vartheta}. \tag{2.31}$$

The generalized eigenvalue problem $\mathbf{W}\mathbf{g} = \omega\mathbf{Z}\mathbf{g}$ can be solved by using the Chebyshev collocation method, where $\mathbf{W}, \mathbf{Z}$ are two matrices, and $\mathbf{g}$ is the eigenvector [33]. N_c Gauss-Lobatto points are set in the flow region $z = (1 - \cos\vartheta_j)/2\vartheta_j = j\pi/(N_c + 1).j = 1 \sim N_c$, while 2 points are set at the boundaries $z = 0,1$. The perturbation quantities are expanded in Chebyshev polynomials as:

$$\widehat{u} = \sum_{k=1}^{N_c+1} s_k H_{k-1}(\widehat{z}). \tag{2.32}$$

here $\widehat{z} = 1 - 2z$, $H_{k-1}(\widehat{z}) = \cos((k-1)\cos^{-1}(\widehat{z}))$ is the $(k-1)-$th Chebyshev polynomial, and s_j is the coefficient. In present work, the results are sufficiently accurate when $N_c = 80$–120. The convergence can be seen in Table 1.

Our computation shows that $\widehat{\psi}(z) = 0$ for the least stable modes. So the variations of S_a and O_h do not change other variables in (2.30)-(2.31), and the results of stability analysis are not sensitive to them.

2.4. Non-modal analysis

As some experiments reported that transition scenarios often highly depend on the level of initial and external disturbances [34], we examine the amplifications of initial disturbances and external forcing by the non-modal approach.

Suppose a perturbation with the wave numbers (α, β) can be represented as a sum of normal modes as follows [35],

$$\boldsymbol{\psi}(z, t) = \sum_j a_j \exp(-i\omega_j t)\boldsymbol{\psi}_j(z). \tag{2.33}$$

here, $\boldsymbol{\psi}(z, t) = (u, v, w, \theta)$ is a vector containing the perturbation velocity and surface-charge density, the subscript j stands for the jth least stable mode, a_j is the jth expansion coefficient, and $\boldsymbol{\psi}_j = (\widehat{u}_j, \widehat{v}_j, \widehat{w}_j, \widehat{\vartheta}_j)$ is the jth eigenvector.

The time evolution of perturbations can be derived as follows,

$$\frac{\partial}{\partial t}\boldsymbol{\psi} = -\mathrm{i}\widehat{\mathbf{L}}\boldsymbol{\psi} + \boldsymbol{\Theta}. \tag{2.34}$$

here, $\widehat{\mathbf{L}} = (\mathbf{Z}')^{-1}\mathbf{W}'$ is an operator with eigenvalues $\{\omega_j\}_{j=1,2\ldots}$ determined by the modal analysis, and $\boldsymbol{\Theta}$ is a input signal with the frequency ω in the form

$$\boldsymbol{\Theta} = \exp[\mathrm{i}(-\omega t + \alpha x + \beta y)]\widehat{\boldsymbol{\Theta}}(z). \tag{2.35}$$

When the background noise is negligible ($\boldsymbol{\Theta} = 0$), the amplification of initial disturbances can be measured by the transient growth function,

$$G(t) = \sup_{\boldsymbol{\psi}(0)\neq 0} \|\boldsymbol{\psi}(t)\|^2 \Big/ \|\boldsymbol{\psi}(0)\|^2, \tag{2.36}$$

which is the greatest possible growth in energy of an initial perturbation at time t. Here, $\|\boldsymbol{\psi}\|$ is the norm of vector $\boldsymbol{\psi}$, which can be defined by the "energy" as follows [35],

Table 1
The eigenvalues of computed by different numbers of nodes.Case1: the linear flow at $R = 800$, $k = 1$ and $\varphi = 0°$; Case2: the return flow at $R = 800$, $k = 1$ and $\varphi = 90°$.

N_c	Case1		Case2	
	$\omega_i(\times 10^{-2})$	$\omega_r(\times 10^{-2})$	$\omega_i(\times 10^{-3})$	ω_r
80	−2.48537	2.50235	−4.33425	0
100	−2.48537	2.50235	−4.33425	0
120	−2.48539	2.50236	−4.33426	0

$$E = \|\boldsymbol{\psi}\|^2 = \int \left(|u|^2 + |v|^2 + |w|^2\right) d^3r + \varsigma \int \left(|\vartheta|^2\right) d^2r. \tag{2.37}$$

$\int f \cdot d^3r$and $\int f \cdot d^2r$ stand for the integration of function f on the volume and surface, respectively. $\varsigma$is a positive coefficient. As no electric potential perturbation is found in the modal analysis, ψ is not included in (2.37).

It can be derived from (2.34), (2.35) that the response $\boldsymbol{\psi}$ has the solution

$$\boldsymbol{\psi} = \mathrm{i}\left(\omega \mathbf{I} - \widehat{\mathbf{L}}\right)^{-1} \exp[\mathrm{i}(-\omega t + \alpha x + \beta y)]\widehat{\boldsymbol{\Theta}}, \tag{2.38}$$

where$\mathbf{I}$is the identity matrix and the solution operator $(\omega \mathbf{I} - \widehat{\mathbf{L}})^{-1}$is the resolvent [33]. Thus, the amplification of external forcing is measured by the response function,

$$\Re(\omega) = \max_{\boldsymbol{\Theta} \neq 0} \|\boldsymbol{\psi}\| / \|\boldsymbol{\Theta}\| = \left\| \left(\omega \mathbf{I} - \widehat{\mathbf{L}}\right)^{-1} \right\|, \tag{2.39}$$

which is the maximum value of amplification to external excitations.

In the computation, the transient growth and response functions can be obtained by using the first K modes,

$$\boldsymbol{\psi}(z,t) \approx \sum_{j=1}^{K} a_j \exp(-i\omega_j t) \left(\widehat{u}_j, \widehat{v}_j, \widehat{w}_j, \widehat{\vartheta}_j\right). \tag{2.40}$$

The convergent results of$G(t)$and $\Re(\omega)$are obtained when K is large enough [33],

$$G(t) \approx \left\| \mathbf{F} \exp(-\mathrm{i}\boldsymbol{\Lambda}_K t) \mathbf{F}^{-1} \right\|_2^2, \tag{2.41}$$

$$\Re(\omega) = \left\| \left(\omega \mathbf{I} - \widehat{\mathbf{L}}\right)^{-1} \right\| \approx \left\| \mathbf{F} (\omega \mathbf{I} - \boldsymbol{\Lambda}_K)^{-1} \mathbf{F}^{-1} \right\|_2. \tag{2.42}$$

here, $\boldsymbol{\Lambda}_K = \mathrm{diag}(\omega_1, \omega_2 \ldots \omega_K)$, $\mathbf{F}$ is a decomposition of a Hermitian matrix$\mathbf{A} = \mathbf{F}^* \mathbf{F}$, where $\mathbf{F}^*$ is the Hermitian conjugate of $\mathbf{F}$, and$\mathbf{A}$is the matrix defined in terms of a inner product,

$$A_{jl} = (\boldsymbol{\psi}_j, \boldsymbol{\psi}_l) = \int \left(\widehat{u}_j^* \widehat{u}_l + \widehat{v}_j^* \widehat{v}_l + \widehat{w}_j^* \widehat{w}_l\right) d^3r + \varsigma \int \left(\widehat{\vartheta}_j^* \widetilde{\vartheta}_l\right) d^2r. \tag{2.43}$$

The definition of 2-norm in (2.41)and (2.42) is$\|\mathbf{H}\|_2 = \sup_{\kappa \neq 0} \|\mathbf{H}\kappa\|^2 / \|\kappa\|^2$, where, $\kappa$is a vector and $\mathbf{H}$ is a matrix.

The choice of ς is arbitrary. However, we expect that both the velocity and surface-charge density have large amplifications. In addition, $\int (|u|^2 + |v|^2 + |w|^2) d^3r >> \varsigma \int (|\vartheta|^2) d^2r$, which means that the disturbance energy in (2.37) is mainly a measure of kinetic energy. So the value$\varsigma = 10^{-3}$is chosen. It is found that the results will not change qualitatively when ς is the order of 10^{-3}.

3. Numerical results

3.1. Modal stability analysis

In the modal analysis, we compute the growth rate ω_i of the least stable modes at different Reynolds numbers. However, both the return flow and the linear flow are stable at all Reynolds numbers, which seems unrealistic. This indicates that the modal analysis is insufficient, and there is a need to examine the sensitivity of flow to initial condition and background noise by the non-modal approach.

3.2. Non-modal stability

In the non-modal analysis, we compute the transient growth function $G(t)$ and response function $\Re(\omega)$. The maximum transient growth and response are defined as

$$G^{\max}(\alpha,\beta) = \max_{t \geq 0} G(\alpha,\beta,t), \quad \Re^{\max}(\alpha,\beta) = \max_{\omega \in \mathbf{R}} \Re(\alpha,\beta,\omega). \tag{3.1}$$

$t^{\max}$ is the optimal time corresponding to $G^{\max}$. Then, the optimal growth and response are defined as

$$G^{\mathrm{opt}} = \max_{\alpha,\beta} G^{\max}(\alpha,\beta), \quad \Re^{\mathrm{opt}} = \max_{\alpha,\beta} \Re^{\max}(\alpha,\beta). \tag{3.2}$$

Due to symmetry, we shall confine ourselves to the cases:$\alpha \geq 0$, $\beta \geq 0$.

3.2.1. Maximum growth

We examine the maximum transient growth $G^{\max}$with various wavenumbers. The level lines of $G^{\max}$ in the $\alpha - \beta$ plane are displayed in Fig. 3, which shows that the transient growth of the linear flow is more obvious than that of the return flow. The optimal growth appears near the spanwise direction ($\varphi = 90^\circ$), which is similar to the cases in thermocapillary layers [19] and channel flows [35]. However, the maximum growth of linear flow is much smaller than that of plane Couette flow at the same R, although their velocity distributions are the same.

3.2.2. Transient growth function

The growth functions $G(t)$ and $G^{\max}$ for streamwise-independent disturbances ($\varphi = 90^\circ$) are displayed in Fig. 4. It can be seen that the perturbation experiences an obvious transient growth and then decays when the time is large enough. $G^{\max} \propto R^2$for two flows.

3.2.3. Flow field corresponding to the maximum growth

The flow fields corresponding to the maximum growth for the linear flow are displayed in Fig. 5. There are large transient growths for both the perturbation velocity and the surface-charge density. The growth is mainly caused by the amplification of $|u|$, whose amplitude appears in the middle of the layer. There are counter-rotating vortices and streamwise streaks at both $t = 0$ and $t = t^{\max}$. There are two rolls in the vertical direction at $t = 0$, while one roll is found at $t = t^{\max}$. It seems that there is no phase difference between the surface-charge densities at these two times: $|\arg[\vartheta(t = 0)] - \arg[\vartheta(t = t^{\max})]| \approx 0^\circ$. The flow fields of return flow is similar to Fig. 5.

3.2.4. Response function

The level lines of the logarithm of$\Re^{\max}$in the $\alpha - \beta$ plane are plotted in Fig. 6. It shows that $\Re^{\max}$could reach O (1000) for a wide range of wave-numbers. The optimal response appears in the spanwise direction ($\alpha = 0$).

In order to show the largest amplification of external disturbance at different real frequencies, we display the variation of response function$\Re$with ω for the return flow in Fig. 7. It can be seen that the case at $\varphi = 90^\circ$ is very different from that at $\varphi = 0^\circ$. When $\varphi = 90^\circ$, $\Re^{\max}$is reached at $\omega = 0$and $\Re^{\max} \propto R^2$. However, when $\varphi = 0^\circ$, there are many peaks in the curve of $\Re(\omega)$. $\Re^{\max}$Decreases with k, and the frequency corresponding to $\Re^{\max}$changes with k. The properties of $\Re(\omega)$ for the linear flow are similar.

3.2.5. Input and output fields

The perturbation fields corresponding to maximum responses are displayed in Figs. 8 and 9. It can be found that there are large amplifications for both the perturbation velocity and the surface-charge density. For the streamwise-independent disturbance ($\varphi = 90^\circ$) in Fig. 8, the flow fields are similar to those of transient growth in Fig. 5. However, the phase difference between the input and output is $\left|\arg(\vartheta_{\mathrm{input}}) - \arg(\vartheta_{\mathrm{output}})\right| \approx 90^\circ$. For the spanwise-independent disturbance ($\varphi = 0^\circ$) in Fig. 9, the vortices are spanwise. In both cases, the streamwise velocity is amplified significantly. The amplitude of streamwise velocity appears in the middle of the layer at $\varphi = 90^\circ$, while it appears on the surface at $\varphi = 0^\circ$.

3.2.6. Pseudospectrum

The reason why the disturbance could be amplified substantially in subcritical flows can be attributed to the non-normality of the operator

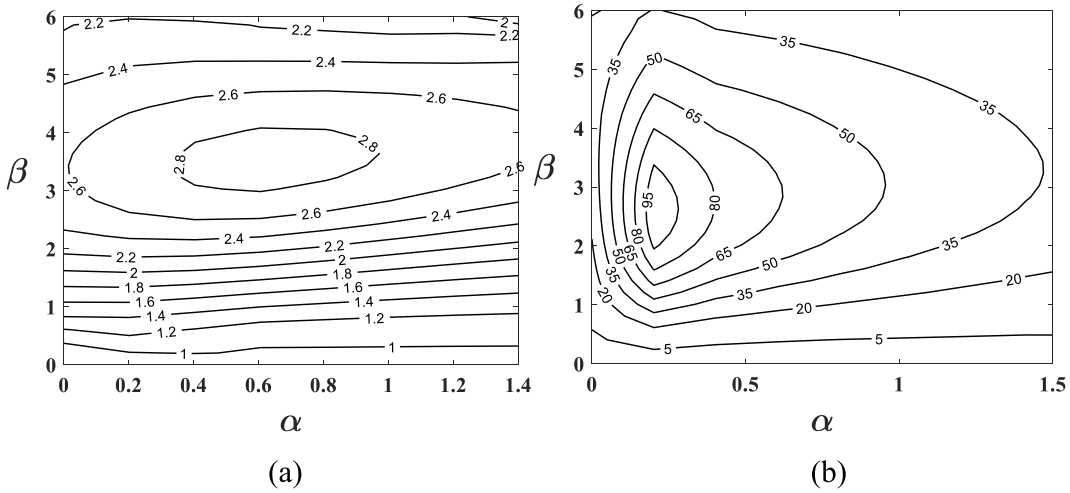

Fig. 3. Level lines of the maximum growth $G^{\max}$ in the $\alpha-\beta$ plane at $R = 800$ for: (a) the return flow; (b) the linear flow.

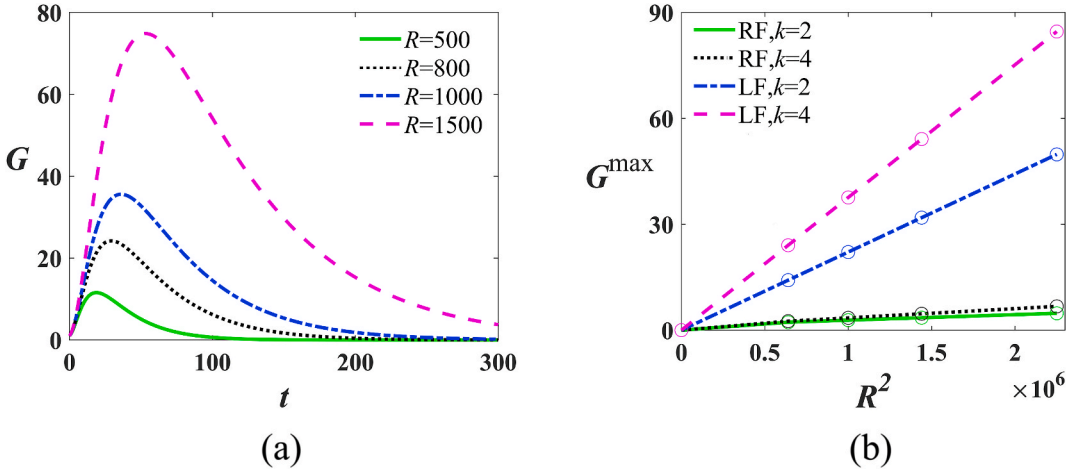

Fig. 4. (a) The variation of $G(t)$ with time for the linear flow with various Reynolds numbers R at $k = 4$ and $\varphi = 90^{\circ}$; (b) The variation of $G^{\max}$ with R^2. RF and LF stand for the return flow and the linear flow, respectively.

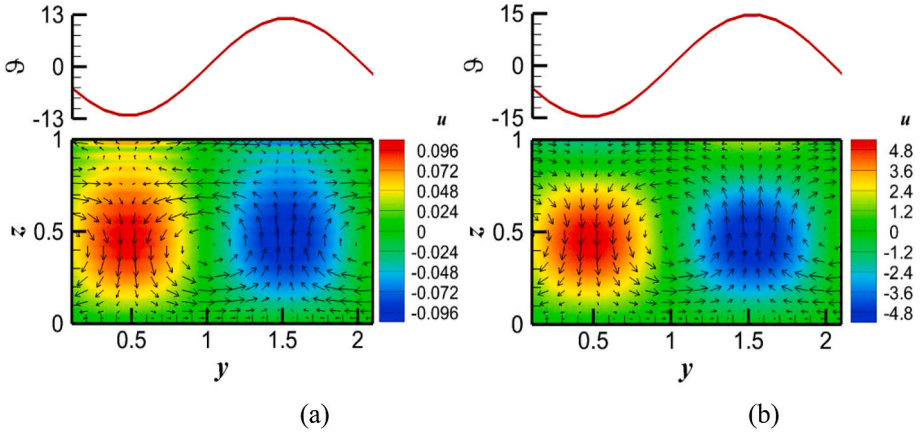

Fig. 5. The flow fields corresponding to the maximum growth for the linear flow at $R = 800$, $\varphi = 90^{\circ}$, $k = 3$: (a) the flow field at the initial time; (b) the flow field at $t^{\max} = 29$. The maximum growth is $G^{\max} = 24.2$. At the initial time, the amplitudes are $|u| = 0.0993$,$|v| = 0.9743$, $|w| = 0.5859$and $|\vartheta| = 12.0372$, while at $t^{\max} = 29$, $|u| = 5.2483$,$|v| = 0.1616$, $|w| = 0.1529$and $|\vartheta| = 14.5593$.

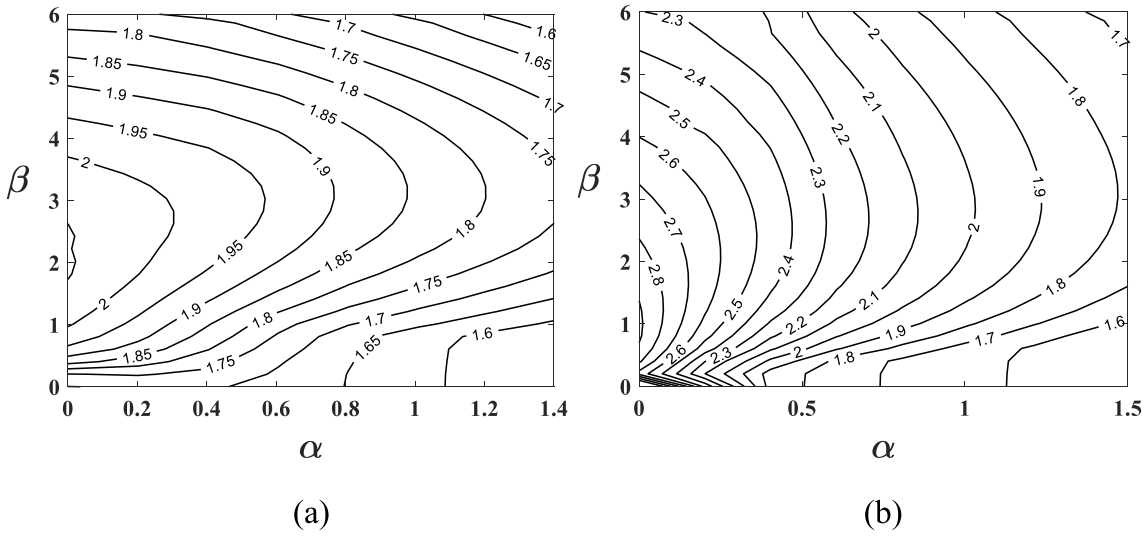

Fig. 6. Level lines of the logarithm of the maximum response $\Re^{max}$ in the $\alpha - \beta$ plane at $R = 800$ for (a) the return flow; (b) the linear flow.

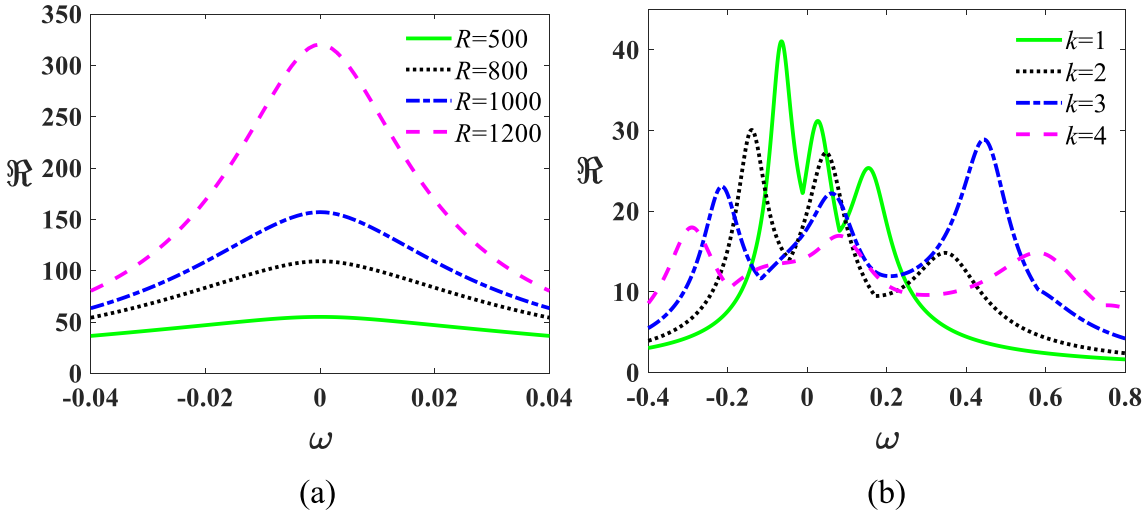

Fig. 7. The response function $\Re$ versus the real frequency for the return flow at: (a) $k = 3$, $\varphi = 90°$; (b) $R = 800$, $\varphi = 0°$.

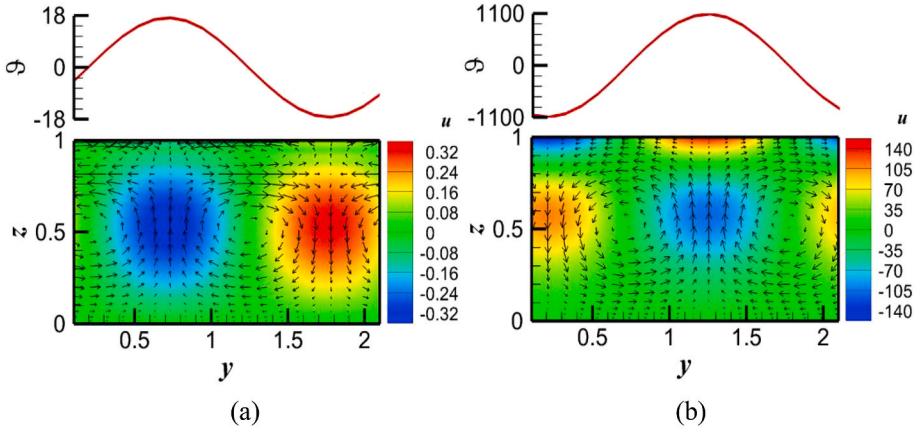

Fig. 8. The perturbation fields corresponding to the maximum response for the return flow at $R = 800$, $k = 3$ and$\varphi = 90°$: (a) the input field; (b) the output field. The maximum response is $\Re^{max} = 109.3$ at $\omega = 0$. The amplitudes of input are $|u| = 0.3351$,$|v| = 1.1146$, $|w| = 0.4718$and $|\vartheta| = 17.2695$, while the amplitudes of output are $|u| = 147.9951$,$|v| = 12.1695$, $|w| = 12.0197$and $|\vartheta| = 1090.7$.

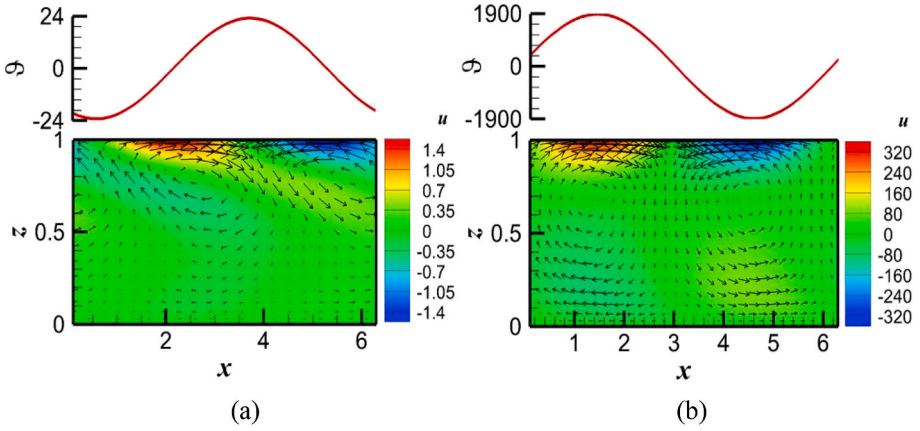

Fig. 9. The perturbation fields corresponding to the maximum response for the return flow at $R = 800$, $k = 1$ and $\varphi = 0^{\circ}$: (a) the input field; (b) the output field. The maximum response is $\Re^{\max} = 41.1$ at $\omega = -0.065$. The amplitudes of input are $|u| = 1.5415$, $|v| = 0$, $|w| = 0.1481$and $|\vartheta| = 23.1544$, while the amplitudes of output are $|u| = 337.5273$, $|v| = 0$, $|w| = 40.6759$and $|\vartheta| = 1885.1$.

$\widehat{\mathbf{L}} = (\mathbf{Z}')^{-1}\mathbf{W}'$, whose eigenfunctions are non-orthogonal. The extent of non-normality can be seen from its pseudospectrum [20],

$$\Lambda_{\varepsilon}\left(\widehat{\mathbf{L}}\right) = \left\{\omega \in \mathrm{C} : \left\|\left(\omega\mathbf{I} - \widehat{\mathbf{L}}\right)^{-1}\right\| \geq \varepsilon^{-1}\right\}, \varepsilon > 0, \tag{3.3}$$

which demonstrates the response to external forcing with complex frequencies and also assesses the susceptibility of eigenvalues to disturbances. If the contours for $\varepsilon << 1$ are visible on an O (1) scale, then $\widehat{\mathbf{L}}$is highly non-normal [36].

In Fig. 10, the eigenvalues and isolines of pseudospectra are displayed. When$\varphi = 90^{\circ}$, most eigenvalues are located in the imaginary

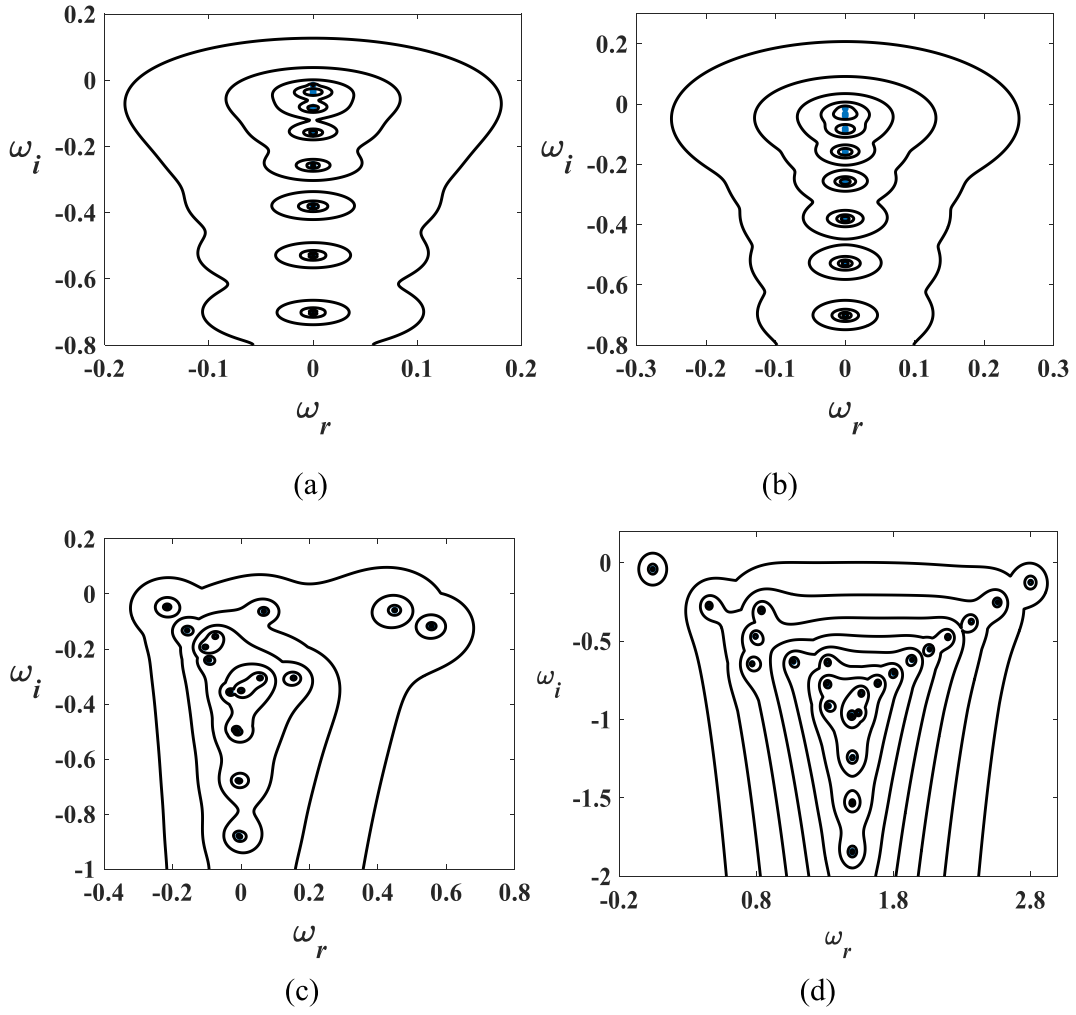

Fig. 10. Pseudospectra at $R = 4000$, $k = 4$: (a) the return flow at $\varphi = 90^{\circ}$; (b) the linear flow at $\varphi = 90^{\circ}$; (c) the return flow at $\varphi = 0^{\circ}$; (d) the linear flow at $\varphi = 0^{\circ}$.: eigenvalues; —: contours from outermost to innermost representing levels from$\varepsilon = 10^{-1}$ to 10^{-6}(the spacing of the exponent is 0.5).

axis $w_r = 0$. The contours are visible on an $O(1)$ scale for $\varepsilon = 10^{-1.5}$, so the non-normality of the operator is moderate. Comparing with the eigenvalues of thermocapillary layers, we can find that there is a pair of eigenvalues with $w_r \neq 0$ near the real axis in the former [37], which cannot be found in Fig. 10. The cases of return flow and linear flow are similar, which suggests that the basic flow has little impact on the pseudospectra at $\varphi = 90^{\circ}$.

When$\varphi = 0^{\circ}$, the spectrum displays a 'Y'-shaped structure, which is similar to the spectrum of OS operator in channel flows [35]. The middle part of 'Y'-shaped spectrum are located near the imaginary axis $w_r = 0$and $w_r = 1.5$ for the return flow and the linear flow, respectively. The wave speeds of these modes are $c = w_r/k = 0$and $c = 0.5$, which are the same as the average velocities of their basic flows. The contours are visible on an $O(1)$ scale for the return flow and the linear flow at $\varepsilon = 10^{-2}$and $\varepsilon = 10^{-4}$, respectively. So the operator of linear flow is highly non-normal and the eigenvalues are highly susceptible to the disturbances. The pseudospectrum at $\varphi = 0^{\circ}$ is sensitive to the basic flow.

4. Discussion

We will discuss the properties of perturbation and the instability mechanism in this section. Comparisons are made with channel flows and thermocapillary layers.

In the modal analysis, our computation suggests that the electric potential perturbation is always zero for the least stable modes. The reason can be explained as follows. Suppose a perturbation of electric potential$\psi'$is added to the basic flow, it can only decay quickly, which can be seen from two aspects. First, there is no convection of charge density in the region $0 \leq z < 1$, so no mechanism can increase the amplitude of ψ'. Second, the Ohmic conduction induced by $\nabla\psi'$always makes ψ'decay. Similar to the relaxation of free-charge density [7], we can estimate the variation of $\psi'$with time as$\exp(\omega_i t)$, where $\omega_i \sim -t_s/\tau$, $t_s = d/\widetilde{U}$is the time scale of flow and $\tau = \varepsilon/\sigma$ is the relaxation time. As$\tau << t_s$, there is a fast decay of ψ'. For our estimated parameters, $\tau \tilde{} 1.59 \times 10^{-4}st_s \tilde{} 0.336$s, $\omega_i \sim -2113$. So this mode is unimportant in the stability analysis. On the contrary, if the mode does not decay rapidly, it must have $\psi' = 0$.

The time evolution of perturbation kinetic energy is [38],

$$\begin{aligned}\frac{\partial E_k}{\partial t} = -\frac{1}{2R}\int(\boldsymbol{\tau}:\mathbf{S})d^3r + \frac{1}{R}\int \mathbf{u}\cdot\boldsymbol{\tau}\cdot\mathbf{n}d^2r - \int \mathbf{u}\cdot((\mathbf{u}\cdot\nabla)\mathbf{u}_0)d^3r \\ + \int \mathbf{u}\cdot\mathbf{F}^{in}d^3r \\ = -N + M + I + \Psi,\end{aligned} \tag{4.1}$$

where $\mathbf{F}^{in}$is the input force, N is the work done by the perturbation stress, M is the work done by shear stress on the surface and I is the interaction between the perturbation and basic flow. For Newtonian fluid, the stress is proportional to the strain rate, so N stands for the viscous dissipation $(N > 0)$.

Table 2 shows the terms of (4.1) for the disturbance corresponding to the maximum growth in Fig. 5, which are normalized by the kinetic energy

$$2E_{kin} = \int |\mathbf{u}|^2 d^3r = 1. \tag{4.2}$$

It can be seen that at the initial time, $I + M > N$, so a transient growth occurs. However, all terms (I, M and N) decrease with time. I and M decrease more rapidly than N. When $t > t^{\max} = 29$, the perturbation kinetic energy decays. In the linear flow, I is the main energy source, while M is very small. However, we find that both I and M are important in the return flow. The terms of (4.1) for the disturbance corresponding to the maximum response are displayed in Table 3. Similar results are found for the perturbation at $\varphi = 90^{\circ}$. On the contrary, when $\varphi = 0^{\circ}$(Fig. 9), the perturbation energy mainly comes from M, while I leads to the dissipation.

In the non-modal approach, the perturbation is expressed as the sum of normal modes in (2.33). Table 4 shows the eigenvalues, the surface-charge density and the expansion coefficients in (2.33) of the least stable modes for the perturbation in Fig. 5. It can be seen that there are two kinds of modes. The first one is purely hydrodynamic, as its surface-charge density is zero. On the contrary, the second one is electro-hydrodynamic as $|\vartheta| \neq 0$. Both of them are important in the non-modal stability. There are perturbations of surface-charge density in Figs. 5, Figs. 8and 9.

Comparing the thermocapillary liquid layer with the electrocapillary one, we can find that their basic flows are exactly the same. However, there are three differences between them. First, there are perturbations of temperature in the flow region for the former, while for the latter, the charge density perturbation only appears on the surface. Second, critical Reynolds numbers are found for the former, while the latter is always stable. Third, the non-modal stability changes with the Prandtl number for the former [38], while the energy mechanism depends on the basic flow and propagation angle for the latter.

The velocity distribution of plane Couette flow is the same as that of linear flow. However, when $R = 2000$, $G^{\text{opt}} \approx 1170$for plane Couette flow [24], while $G^{\text{opt}} \approx 462$ for the electrocapillary linear flow, and $G^{\max}$of thermocapillary linear flow depends on Pr and the Biot number Bi. These differences are due to their boundary conditions. We restrict our attention to the case at $\varphi = 90^{\circ}$, which corresponds to the optimal growth and response functions. For channel flows, the boundary conditions for velocities are non-slip:$u = v = 0$. For thermocapillary flows, the transient growth increases with Bi at small Prandtl numbers [19]. When $Bi \to \infty$, there is no perturbation of shear stress, so $Du = Dv = 0$. On the contrary, for electrocapillary convections, we have $Du = \vartheta, Dv = 0$.

The amplification of streamwise-independent disturbance ($\varphi = 90^{\circ}$) is caused by the streamwise vortices (see Figs. 5and 8). They can absorb energy from the basic flow by the "lift-up" effect [24,38]:

$$\frac{\partial u}{\partial t} + w \cdot DU_0 \approx 0, \tag{4.3}$$

where the streamwise velocity increases with time in the middle of the layer. Meanwhile, the surface-charge induced by the convection of streamwise vortices leads to the electrocapillary force, which also excites the streamwise streaks in the return flow. For the spanwise-

Table 2
The terms of (4.1) for the disturbance corresponding to the maximum growth in Fig. 5.

t	0	10	20	29	40
N	0.082199	0.036783	0.032985	0.030307	0.027232
M	0.011294	0.009891	0.005159	0.002639	0.001227
I	0.157229	0.083527	0.040898	0.027760	0.019739
$\frac{\partial E_{kin}}{\partial t}$	0.086325	0.056636	0.013071	0.000092	−0.006266

Table 3
The terms of (4.1) for the disturbance corresponding to the maximum response. Cases 1–2 correspond to the cases in Fig. 8–9, respectively. Case 3 corresponds to the case in the linear flow at $R = 800$, $k = 3$ and $\omega = 0$.

	Case 1 (RF, $\varphi = 90^{\circ}$)	Case 2 (RF, $\varphi = 0^{\circ}$)	Case 3 (LF, $\varphi = 90^{\circ}$)
N	0.065480	0.057139	0.020931
M	0.037612	0.065629	−0.000770
I	0.024414	−0.005408	0.021642
Ψ	0.003454	−0.003082	0.000059

Table 4
The eigenvalues, surface-charge density and expansion coefficients of the least stable modes for the perturbation in Fig. 5.

$\mathrm{Im}(\omega)_j$	$\widehat{\vartheta}_j$	a_j
−0.014334	0	0.238603
−0.032012	−34.2469 + 1.99425i	0.252283–1.23256i
−0.039008	0	−0.123125-1.14753i
−0.081008	−8.86957 + 21.9536i	−0.992038 + 0.243313i
−0.088356	0	−0.863026 + 0.463308i
−0.154937	−20.5026-0.931008i	−0.014915 + 0.151272i
−0.162378	0	0.175806 + 0.265931i

independent disturbances ($\varphi = 0^{\circ}$), the electrocapillary effect is crucial for the amplification. However, the input force is also indispensable, as the perturbation cannot be self-sustained.

The modal analysis suggests that all modes are stable, so the perturbation similar to Tollmien-Schlichting (TS) waves may not be observed in the transition of electrocapillary layers. Instead, the perturbations predicted by the non-modal approach are more likely to be found in experiments. As the most amplified disturbance is nearly streamwise-independent, we could expect that when a perturbation is added in the electrocapillary layer, there will be streamwise elongated structures in the flow field with an obvious fluctuation in the surface-charge density. However, due to the small bulk relaxation time, the perturbation of electric field is negligible.

The basic flows considered in this work could appear in many shear flows driven by electrocapillary force, such as the liquid film in electrokinetic systems [39] and droplet motion [40]. The linear flow is a simple model for the liquid layer with no pressure gradient in the streamwise direction, while the return flow corresponds to the convection with two ends. When the electrocapillary flow becomes unstable, its controllability will be reduced significantly. The stability analysis of these two flows could capture the main physical aspects of convective instability in the electrocapillary convection, which not only improves our understanding of electrohydrodynamics, but also is useful in the applications.

5. Conclusion

The linear stability of electrocapillary liquid layers is examined by the modal and non-modal approaches. The sensitivities of basic flow to initial condition and background noise are examined by the transient growth and the response functions, respectively.

The modal analysis shows that there is no electric potential perturbation. Thus, the current perturbation caused by the Ohmic conduction is also zero. Two kinds of modes are found, which are the purely hydrodynamic mode and the electrohydrodynamic one. The latter has the surface-charge density, which cannot be found in the former. Both the return flow and the linear flow are stable at all Reynolds numbers.

In the non-modal approach, both the perturbation velocity and the surface-charge density can be amplified significantly. Both the optimal growth and response are proportional toR^2 and appear near the spanwise direction ($\varphi = 90^{\circ}$). For the transient growth, there is no phase difference for the surface-charge densities at the initial and optimal times: $|\arg[\vartheta(t=0)] - \arg[\vartheta(t=t^{\max})]| \approx 0^{\circ}$. However, for the optimal response, the phase difference between the input and output has $\left|\arg(\vartheta_{\mathrm{input}}) - \arg(\vartheta_{\mathrm{output}})\right| \approx 90^{\circ}$.

For streamwise-independent disturbances ($\varphi = 90^{\circ}$), the pseudospectra of return flow and linear flow are similar, while the non-normality of evolution operator is moderate. Most modes have zero frequency. For the linear flow, the main energy source of perturbation is the basic flow, while for the return flow, both the basic flow and electrocapillary force are important in the energy mechanism. On the contrary, for spanwise-independent disturbances ($\varphi = 0^{\circ}$), the pseudospectra are sensitive to the basic flow while the evolution operator is highly non-normal. There are many modes whose wave speeds are equal to the average velocities of their basic flows. The perturbation energy mainly comes from the work done by electrocapillary force.

Data availability

The data that supports the findings of this study are available within the article.

Declaration of competing interest

The authors declare that they have no known competing financial interests or personal relationships that could have appeared to influence the work reported in this paper.

Acknowledgments

This work has been supported by the National Natural Science Foundation of China (Nos.11872032, 11832013 and 11772344), Zhejiang Provincial Natural Science Foundation (No.LY21A020006), K. C. Wong Magna Fund and the Special research funding from the Marine Biotechnology and Marine Engineering Discipline Group in Ningbo University(No. 422004582). The authors also gratefully acknowledge the referees for their helpful comments.

References

[1] D.A. Saville, Electrohydrodynamics: the Taylor-Melcher leaky dielectric model, Annu. Rev. Fluid Mech. 29 (1) (1997) 27–64.
[2] F. Liu, C.H. Chen, Electrohydrodynamic cone-jet bridges: stability diagram and operating modes, J. Electrost. 72 (4) (2014) 330–335.
[3] X. Li, J. Deng, D. Ge, H. Yue, Rapid crystallization of electrohydrodynamically atomized ZrO2 thin films by laser annealing, Appl. Surf. Sci. (2020) 145510.
[4] A. Ahmadi, J.F. Holzman, H. Najjaran, M. Hoorfar, Electrohydrodynamic modeling of microdroplet transient dynamics in electrocapillary-based digital microfluidic devices, Microfluid. Nanofluidics 10 (5) (2011) 1019–1032.
[5] W. Hassen, M.N. Borjini, H.B. Aissia, Enhanced heat transfer by unipolar injection of electric charges in differentially heated dielectric liquid layer, Fluid Dynam. Mater. Process. 8 (4) (2012) 381–396.
[6] W. Hassen, L. Kolsi, H.F. Oztop, A. Al-Rashed, M.N. Borjini, K. Al-Salem, Electro-thermo-capillary-convection in a square layer of dielectric liquid subjected to a strong unipolar injection, Appl. Math. Model. 63 (2018) 349–361.
[7] J.R. Melcher, G.I. Taylor, Electrohydrodynamics: a review of the role of interfacial shear stresses, Annu. Rev. Fluid Mech. 1 (1) (1969) 111–146.
[8] D.T. Papageorgiou, Film flows in the presence of electric fields, Annu. Rev. Fluid Mech. 51 (2019) 155–187.
[9] H. González, D.S. Néron G, J.P. Chabrerie, Influence of bounded geometry on electrocapillary instability, Phys. Rev. B 50 (4) (1994) 2520.
[10] A.B. Petrin, Electrocapillary instability of a conducting liquid cylinder, J. Exp. Theor. Phys. 106 (5) (2008) 963–973.
[11] L. Mkrtchyan, A. Zakinyan, Y. Dikansky, Electrocapillary instability of magnetic fluid peak, Langmuir 29 (29) (2013) 9098–9103.
[12] H. González, D.S. Néron G, J.P. Chabrerie, Influence of bounded geometry on electrocapillary instability, Phys. Rev. B 50 (4) (1994) 2520.
[13] L.M. Carrión, M.A. Herrada, J.M. Montanero, Influence of the dynamical free surface deformation on the stability of thermal convection in high-Prandtl-number liquid bridges, Int. J. Heat Mass Tran. 146 (2020) 118831.
[14] S.H. Davis, Thermocapillary instabilities, Annu. Rev. Fluid Mech. 19 (1) (1987) 403–435.
[15] R.J. Riley, G.P. Neitzel, Instability of thermocapillary–buoyancy convection in shallow layers. Part 1.Characterization of steady and oscillatory instabilities, J. Fluid Mech. 359 (1998) 143–155.
[16] Y.R. Li, N. Imaishi, T. Azami, T. Hibiya, Three-dimensional oscillatory flow in a thin annular pool of silicon melt, J. Cryst. Growth 260 (2004) 28–41.
[17] M. Wanschura, V. Shevtsova, H. Kuhlmann, H. Rath, Convective instability mechanisms in thermocapillary liquid bridges, Phys. Fluids 7 (1995) 912–925.
[18] C.Y. Yan, K.X. Hu, Q.S. Chen, Thermocapillary instabilities of liquid layers on an inclined plane, Phys. Fluids 30 (8) (2018), 082101.
[19] K.X. Hu, S. Zheng, Q.S. Chen, Transient growth in thermocapillary liquid layers, Phys. Rev. Fluids 5 (2020), 014001.
[20] L.N. Trefethen, A.E. Trefethen, S.C. Reddy, T.A. Driscoll, Hydrodynamic stability without eigenvalues, Science 261 (1993) 578–584.
[21] S.J. Kline, W.C. Reynolds, F.A. Schraub, P.W. Runstadler, The structure of turbulent boundary layers, J. Fluid Mech. 30 (1967) 741–773.
[22] O. Kiton, K. Nakabyashi, F. Nishimura, Experimental study on mean velocity and turbulence characteristics of plane Couette flow: low-Reynolds-number effects and large longitudinal vortical structure, J. Fluid Mech. 539 (2005) 199–227.

[23] C. Nouar, N. Kabouya, J. Dusek, M. Mamou, Modal and non-modal linear stability of the plane Bingham–Poiseuille flow, J. Fluid Mech. 577 (2007) 211–239.
[24] R. Liu, Q.S. Liu, Non-modal instability in plane Couette flow of a power-law fluid, J. Fluid Mech. 676 (2011) 145–171.
[25] M. Zhang, I. Lashgari, T.A. Zaki, L. Brandt, Linear stability analysis of channel flow of viscoelastic Oldroyd-B and FENE-P fluids, J. Fluid Mech. 737 (2013) 249–279.
[26] M. Zhang, F. Martinelli, J. Wu, P. Schmid, M. Quadrio, Modal and non-modal stability analysis of electrohydrodynamic flow with and without cross-flow, J. Fluid Mech. 770 (2015) 319–349.
[27] K.X. Hu, S. Zheng, Q.S. Chen, Transient growth in thermocapillary liquid layers, Phys. Rev. Fluids 5 (2020), 014001.
[28] M. Teitel, D. Schwabe, A.Y. Gelfgat, Experimental and computational study of flow instabilities in a model of Czochralski growth, J. Cryst. Growth 310 (2008) 1343–1348.
[29] F. Ma, J. Yang, F. Shi, Z. Wang, Zhang, S. Wang, Silicone based nanofluids containing functionalized graphene nanosheets, Colloids Surf., A 431 (2013) 120–126.
[30] D.S.M. Jose, H. Uwe, Capacitance wire-mesh sensor applied for the visualization of three-phase gas-iquid-liquid flows, Flow Meas. Instrum. 34 (9) (2013) 113–117.
[31] G.I. Taylor, A.D. McEwan, The stability of a horizontal fluid interface in a vertical electric field, J. Fluid Mech. 22 (1) (1965) 1–15.
[32] J.R. Melcher, W.J. Schwarz Jr., Interfacial relaxation overstability in a tangential electric field, Phys. Fluids 11 (1968) 2604–2616.
[33] P.J. Schmid, D.S. Henningson (Eds.), Stability and Transition in Shear Flows, Springer, 2001.
[34] P.J. Schmid, Nonmodal stability theory, Annu. Rev. Fluid Mech. 39 (2007) 129–162.
[35] S.C. Reddy, D.S. Henningson, Energy growth in viscous channel flows, J. Fluid Mech. 252 (1993) 209–238.
[36] J.M. Davis, S.M. Troian, Influence of boundary slip on the optimal excitations in thermocapillary driven spreading, Phys. Rev. E 70 (4) (2004), 046309.
[37] K.X. Hu, M. He, Q.S. Chen, Instability of thermocapillary liquid layers for Oldroyd-B fluid, Phys. Fluids 28 (3) (2016), 033105.
[38] K.X. Hu, S. Zheng, Q.S. Chen, The response to external excitations in thermocapillary liquid layers, Phys. Fluids 33 (2021), 032104.
[39] A.J. Pascall, T.M. Squires, Electrokinetics at liquid/liquid interfaces, J. Fluid Mech. 684 (2011) 163–191.
[40] J. Bae, E. Glogowski, S. Gupta, W. Chen, T. Emrick, T.P. Russell, Effect of nanoparticles on the electrohydrodynamic instabilities of polymer/nanoparticle thin films, Macromolecules 41 (7) (2008) 2722–2726.